


ARTICLE

<https://doi.org/10.1038/s42005-019-0233-6>

OPEN

Multiple scattering theory of non-Hermitian sonic second-order topological insulators

María Rosendo López¹, Zhiwang Zhang^{1,2}, Daniel Torrent³ & Johan Christensen ^{1*}

Topological phases of sound enable unconventional confinement of acoustic energy at the corners in higher-order topological insulators. These unique states which go beyond the conventional bulk-boundary correspondence have recently been extended to non-Hermitian wave physics comprising finite crystal structures including loss and gain units. We use a multiple scattering theory to calculate these topologically trapped complex states that agree very well to finite element predictions. Moreover, our semi-numerical tool allows us to compute the spectral dependence of corner states in the presence of defects, illustrating the limits of the topological resilience of these confined non-Hermitian acoustic states.

¹Department of Physics, Universidad Carlos III de Madrid, Avenida de la Universidad, 28911 Leganés, Madrid, Spain. ²Department of Physics, MOE Key Laboratory of Modern Acoustics, Collaborative Innovation Center of Advanced Microstructures, Nanjing University, 210093 Nanjing, China. ³GROC, UJI, Institut de Noves Tecnologies de la Imatge (INIT), Universitat Jaume I, 12071 Castellón, Spain. *email: johan.christensen@uc3m.es

Topological insulators (TIs) have been extensively studied in condensed matter physics^{1–3} but are also moving forward at fast pace in classical systems such as photonics^{4–7}, acoustics^{8–14}, and mechanics^{15–19}. A key feature of the topological insulators is the existence of robust edge states that are immune to backscattering from disorder or interface variations. Conventionally, the edge states were predicted by the bulk-edge correspondence principle, but recently, the concept of TIs has been generalized to higher-order topological insulators (HOTIs), at which the conventional bulk-boundary correspondence does not apply^{20–24}. Beyond theoretical advances, classical lattices have shown to be a fruitful base since numerous experimental verifications have seen the light of day²⁵ including photonic^{26–28} and phononic crystal systems^{29–36}.

Parity-time \mathcal{PT} symmetry on the other hand, describes the invariance of a non-Hermitian system that can have real eigenvalue spectra despite its complex entities. Those systems are a special kind of physical configurations invariant upon the combined parity \mathcal{P} and time reversal \mathcal{T} operations, which have been realized in artificial structures hosting balanced gain and loss constituents. Systems with \mathcal{PT} -symmetry have been extensively studied in optics and acoustics enabling unusual wave propagation characteristics such as unidirectional invisibility and focusing, as well as complex topological valley-Hall effects^{37–42}.

In this article, we use a multiple scattering theory (MST) to calculate the complex properties of \mathcal{PT} -symmetric second-order topological sonic crystals. Generally speaking, non-Hermitian first-order TIs also have a bulk-boundary correspondence that however has to be modified significantly^{43,44}. Most recently, non-Hermitian HOTIs, as a whole, have been reported owning an even more complex bulk-boundary correspondence^{45–47}.

This paper is a follow up to our short letter⁴⁸, in which all results have been numerically obtained by a commercial finite element method (FEM) solver. Beyond the excellent agreement between the two techniques permitting us to study topological corner, edge and bulk states, as well as their spatial pressure profiles, we deliberately employ the MST to elaborate the robustness of non-Hermitian corner states in the presence of interstitial cylinder-defects.

Results

Multiple scattering theory. We consider a 2D arrangement of N -cylinders located at \mathbf{R}_α , where $\alpha = 1, 2, \dots, N$. These cylinders, made of fluid A with density ρ_a and speed of sound c_a , are embedded in a fluid background with density ρ_b and speed of sound c_b . If an external field P_{in} , with angular frequency ω , impinges the cluster of cylinders, the total scattered field, at a given position \mathbf{r} in polar coordinates (r, θ) , will be given by:

$$P^{\text{sc}}(r, \theta) = \sum_{\alpha=1}^N \sum_q (A_\alpha)_q H_q(kr_\alpha) e^{iq\theta_\alpha}, \quad (1)$$

where H_q is the q^{th} order Hankel function of the first kind, $(r_\alpha, \theta_\alpha)$ are the polar coordinates of the α^{th} cylinder in the reference frame $\mathbf{r}_\alpha = \mathbf{r} - \mathbf{R}_\alpha$, $k = \omega/c_b$ is the wavenumber and $(A_\alpha)_s$ are the coefficients of the scattered field to be determined. The total incident field at the α^{th} cylinder can be expressed either as a linear combination of Bessel functions of the q^{th} order (in a more general approach),

$$P_{\text{in}}(r_\alpha, \theta_\alpha) = \sum_q (B_\alpha)_q J_q(kr_\alpha) e^{iq\theta_\alpha}, \quad (2)$$

or as a sum of the external field P_{in} and the field scattered by all cylinders except the α^{th} one. If we rewrite the latter on a α basis by means of the Graf's addition theorem⁴⁹, we obtain the

following expression:

$$P_\alpha^{\text{in}}(r_\alpha, \theta_\alpha) = \sum_q (A_\alpha)_q J_q(kr_\alpha) e^{iq\theta_\alpha} + \sum_s \sum_{q \neq \alpha} (A_\beta)_s H_{q-s}(kR_{\alpha\beta}) e^{i(s-q)\theta_{\alpha\beta}} J_q(kr_\alpha) e^{iq\theta_\alpha}. \quad (3)$$

Reformulating the equations into matrix form, coefficients $(B_\alpha)_q$ and $(A_\alpha)_q$ of the incident and scattered field, respectively, are related by means of the T-matrix $(A_\alpha)_q = \sum_s (T_\alpha)_{qs} (B_\alpha)_s$. Thus, once we determine the value of the T-matrix, as well as setting the amplitude $(A_\alpha)_q$ of the incident field, we are able to compute the scattered amplitude $(A_\alpha)_q$, by solving the system of linear equations, resulting from substituting Eq. (2) into Eq. (3) and introducing the value of the T-matrix therein. The structure that we are going to study is made of fluid cylinders of circular cross section of radius R_a , whose T-matrix reads:

$$T_q = - \frac{\rho_q J'_q(kR_a) - J_q(kR_a)}{\rho_q H'_q(kR_a) - H_q(kR_a)} \quad (4)$$

$$\rho_q = \frac{\rho_a c_a J_q(k_a R_a)}{\rho_b c_b J'_q(k_b R_a)}.$$

The fluid cylinders are irradiated by an external point source $P_{\text{in}}(r, \theta) = \sum_s H_s(kr_s) e^{is\theta_s}$ located at $\mathbf{R}_s = \mathbf{r} - \mathbf{r}_s$. Rewriting this expression on an α basis allows one to determine the amplitude of the incident field as follows system, $(A_\alpha)_q = H_{s-q}(kR'_s) e^{i(s-q)\theta'_s}$.

Corner states. We begin with a 2D regular Hermitian square sonic crystal with lattice constant a , whose unit cell is composed of four isotropic fluid cylinders embedded in air with an adjacent center-to-center distance $D/a = 0.5$. When adjusting the ratio from $D/a < 0.5$ (shrunk) to $D/a > 0.5$ (expanded), a topological phase transition characterized by the vectorial Zak phase \mathbf{P} emerge. This phase is defined as an integration of the non-Abelian Berry connection \mathbf{A}_{mn} over the first Brillouin Zone (BZ):

$$\mathbf{P} = \iint_{1^{\text{st}} \text{BZ}} dk_1 dk_2 \text{Tr}(\mathbf{A}), \quad \mathbf{A}_{mn} = i \langle u_m | \partial_{\mathbf{k}} | u_n \rangle \quad (5)$$

where $|u_m\rangle$ is the Bloch function for the m^{th} band and m, n run over occupied bands. Due to the C_{4v} symmetry, the previous expression can be rewritten as^{50,51}

$$P_i = \pi \left(\sum_n q_i^n \text{mod} 2 \right), \quad (-1)^{q_i} = \frac{\eta_n(X_i)}{\eta_n(\Gamma)} \quad (6)$$

where i represents the directions x or y , X_i denotes the $X(Y)$ point of the first BZ and η_n stands for the parity of the n^{th} band at the high symmetry point. In a physical context, the Zak phase is related to 2D wave polarization (σ_i with $i = x, y$) through $\sigma_i = P_i/2\pi$. When the origin is chosen to be the center of the metamolecule the Zak phase has only two possible values, 0 or π , with corresponding polarization quantized as 0 and $1/2$ ^{52,53}. In the shrunk scenario, when $D/a < 0.5$ the 2D Zak phase equals $(0, 0)$ with $\sigma = (0, 0)$, indicating a trivial state. In contrary, when the metamolecule is expanded beyond $D/a > 0.5$ the Zak phase equals (π, π) with $\sigma = (\frac{1}{2}, \frac{1}{2})$, indicating a non-trivial state. The coexistence of the non-trivial dipole moments in both directions generate a corner confining state according to the edge-corner correspondence^{22,48,54}. As a result, a corner state is sustained at the 90-degree corners between the trivial and non-trivial regions having non-zero Zak phases in both directions along the interfaces.

Resting on the aforementioned fundamental theory, we construct a finite concentric square crystal (CSC) shown in Fig. 1a, which is based on an inner sonic crystal of size $8a \times 8a$

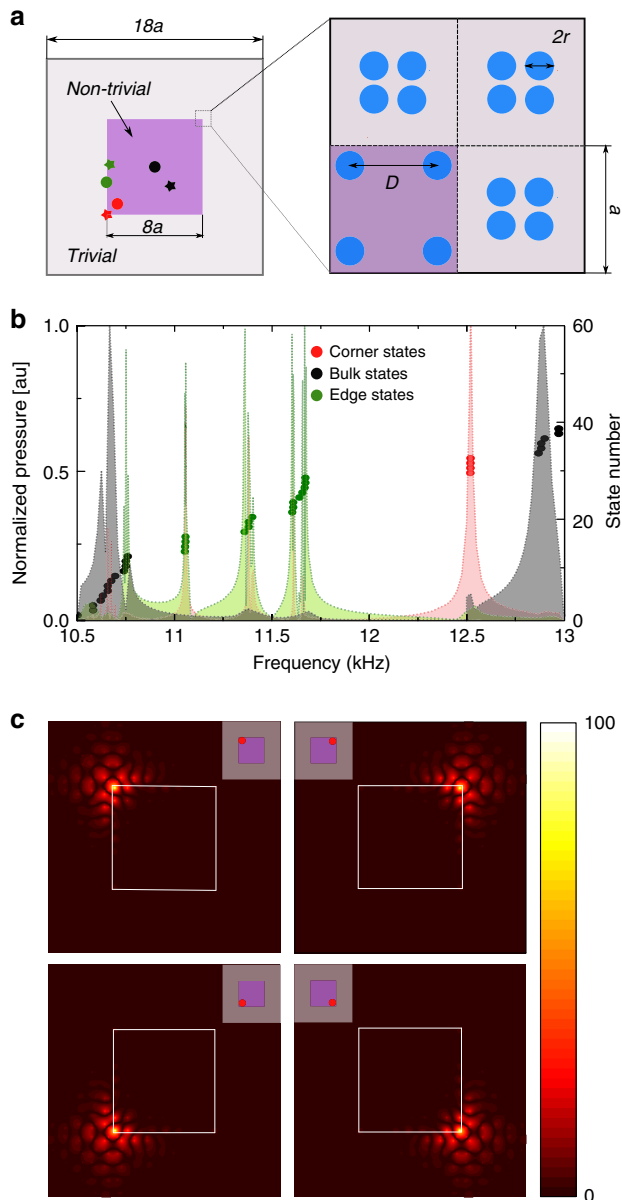


Fig. 1 Hermitian concentric square crystal. **a** Schematic representation of the crystal made of $8a \times 8a$ metamolecule arrays defining the non-trivial region with $D/a = 0.714$ enclosed by a trivial region with $D/a = 0.280$ and thickness $5a$. Circles represent the position of the source exciting the bulk (black), the edge (green) and the corner states (red), which correspondingly are indicated by stars. **b** Comparison between the real eigenfrequencies obtained by finite element method simulations (dots) with the normalized pressure of the excited states from the multiple scattering theory computation. **c** Pressure maps of all corner states. Inserts illustrate the excitation point

constituting the topological non-trivial region with $D/a = 0.714$ that is enclosed by a topological trivial region of width $5a$ and $D/a = 0.280$. As simulations show, indeed we are able to select other ranges of geometrical parameters (see Supplementary Note 1). The lattice constant of the both sonic crystals are taken to be $a = 1$ cm and the radii of the cylinders are $r = 0.12a$. The mass density and the bulk modulus of the background correspond to air, $\rho_0 = 1.21$ kg/m³ and $K_0 = 1.4 \cdot 10^5$ Pa, whereas the mass density and the bulk modulus of the cylinders are $\rho = \rho_0$ and $K = K_0/9$, respectively. Our aim is to employ the MST to obtain the topological corner states of a two-dimensional second-

order topological insulator. In doing this, we first compare the eigenfrequencies calculated with FEMs with the pressure spectrum peaks calculated with a MST. Later on, the MST is also employed to compute pressure field distribution of the corner states. Within the spectral region of the bulk band gap of the periodic crystal⁴⁸, by means of FEM simulations we compute the eigenfrequencies at their corresponding state number of the Hermitian CSC as represented by dots in Fig. 1b. Specifically, we characterize these dots as bulk (black), edge (green) and corner states (red). When conducting the numerical experiment based on the MST we place an acoustic point source at a relevant position of the CSC to computationally be able to measure spectrally the response of the specific confined states. In other words, as corner states confine in the corner, we place the source and probe its excitation near one of the four corners, and schematically represented by dots (sources) and stars (measurement point) in Fig. 1a, we excite and detect the topological edge and bulk states near their origins of the CSC. The spectral pressure responses obtained by the MST and the topological eigenstates from FEM simulations shown in Fig. 1b display a remarkably good agreement. The consistency between the spectral locations obtained by the two distinct methods permits us to faithfully conduct a robust study solely employed by semi-analytical means. Before that, however, we focus on the spatial characteristics of the corner states shown in Fig. 1c. The MST pressure maps visualize equivalent intensity confinement in all of the corners associated to the four possible corner states computed in the spectrum, Fig. 1b. In addition, our predictions display some leakage at the corners enabling sound to penetrate at certain distance into the trivial region. By adjusting its width, the topological confinement can be controlled. However, increasing it would also increase the number of cylinders included in the structure. With a width of $5a$ the total amount of cylinders forming the CSC is 1296, already setting high demands in terms of computation time.

We now study the evolution of the corner states while a total amount of nine interstitial fluid cylindrical defects are gradually introduced. As can be seen in the inset of Fig. 2a, the cylindrical defects are symmetrically located near the upper interface between the non-trivial and the trivial region, and their radii $r = 0.15a$ are slightly larger than the radii of the cylinders forming the CSC, although we chose the same acoustic parameters. As the intensity is the same of all the corner states, a complete study is done by only analyzing the evolution of one of them. Thus, the source is placed in the center of the CSC (red dot in Fig. 2a) and the detection point (red star) is chosen to be located at the upper-right corner between the trivial and the non-trivial region. Corner states are excited in narrow frequency window centered at 12.50 kHz as displayed in Fig. 2b. The results show a slight pressure increase when adding defect up to $n_{\text{defects}} = 3$. Beyond this, a smooth frequency shift together with a slight pressure reduction is predicted when n_{defects} is further increased. For some selected number of interstitial defects as labeled and highlighted by white dots in Fig. 2c, we plot the spatial pressure field maps at their corresponding spectral peaks, clearly displaying the resilience of the corner states in response to a point-like excitation.

We now extend the study of HOTIs to non-Hermitian CSCs by introducing acoustic gain and loss into the metamolecules by employing active acoustic metamaterials. Thus, the complex mass densities of the cylinders are defined as $\rho_{\text{gain}} = (1 + i\beta)\rho_0$ for the gain components and $\rho_{\text{loss}} = (1 - i\beta)\rho_0$ for the lossy ones, while the bulk modulus remain the same as in the Hermitian case, $K = K_0/9$. In order to have an equal amount of loss and gain as measured by the non-Hermiticity parameter β , we construct two types of metamolecules, each having two gain and two loss cylinders. The first non-Hermitian arrangement of the CSC

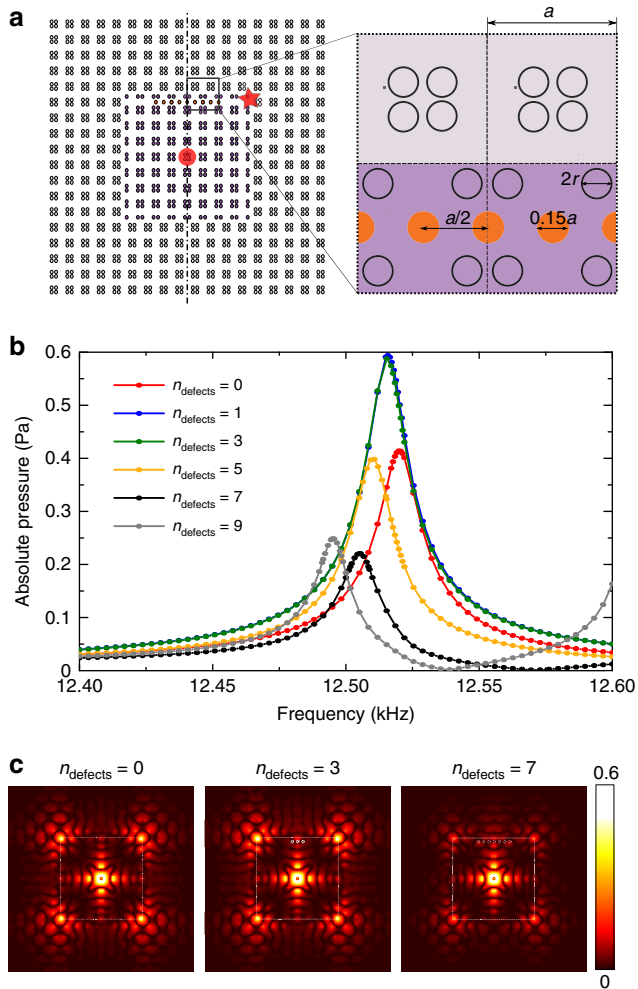


Fig. 2 Study of the topological protection of corner states against perturbations. **a** Schematic representation of the locations of the interstitial defects embedded into the non trivial part of the Hermitian concentric square crystal. **b** Spectral dependence of the pressure at the upper-right corner when the source is placed in the crystal center with a steadily increased number of defects. **c** Mapping the pressure distribution of the corner states in the presence of 0, 3, and 7 defects. In all simulations the source has been placed in the crystal center

introduces symmetrical gain and loss units diagonally distributed as illustrated in Fig. 3a. Notice that gain (loss) cylinders are situated at the diagonal (off diagonal) sites within the trivial region of the CSC and vice versa for the non-trivial part. Figure 3b shows the eigenfrequencies of the CSC containing diagonal non-hermiticity with $\Gamma = 0.03$. Similar to the Hermitian case, the spectral locations of the edge, bulk and corner states obtained by means of the aforementioned numerical experiments agree very well with the eigenfrequencies calculated by FEM. The positions of the sources and measurement points considered for the MST predictions are the same as those considered in the Hermitian CSC as illustrated in Fig. 3a. By comparing Figs. 1b and 3b, we can conclude that the real eigenfrequencies are almost identical in both cases. However, the pressure distribution of the corner states shown in Fig. 3c differs from the one in Fig. 1c, since the pressure is not the same in all of the corners. The states at the off-diagonal corners confine more energy (amplifying) than those at the diagonal sites (attenuating). In particular, the pressure of the attenuating corner states is 60% in comparison to the one confined via the amplifying corner state as Fig. 3d shows.

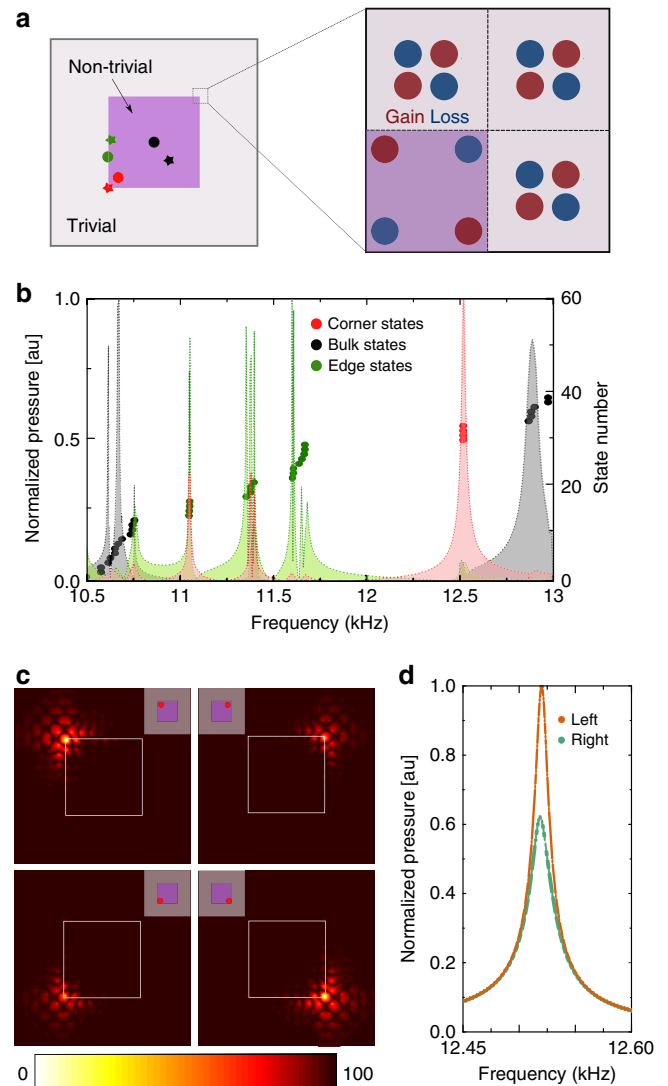


Fig. 3 Concentric square crystal (CSC) with diagonal non-Hermiticity. **a** Magnified view of the CSC displaying the arrangement of the trivial and nontrivial regions. **b** Comparison between the real eigenfrequencies obtained by finite element method simulations (dots) with the normalized pressure of the excited states from the multiple scattering theory computation. **c** Pressure maps of all corner states. Inserts illustrate the excitation point. **d** Pressure difference between the amplifying and attenuating upper corner states

Concerning the study of the robustness in this non-Hermitian configuration, we conduct the same defect study as the one described for the Hermitian case. But now, due to the fact that the pressure of the corner states, as discussed earlier, is asymmetric, the defect analysis has to be undertaken for both the amplifying and the attenuating corner states. Hence, the topological robustness study can be done by focusing only on the upper two corners as depicted in the insets of Fig. 4a, b. Again, the analysis comprises in steady increase of the number of interstitial defect cylinders n_{defects} . Both corner states display a remarkable durability against defects, though unlike the Hermitian case, the present non-Hermitian corner states display slightly differing shifts and pressure drops when n_{defects} increases as seen in the two spectra in Fig. 4. The pressure field maps in Fig. 4c also confirms the pertinacity against defects where opposite corners appear with slightly different pressure values.

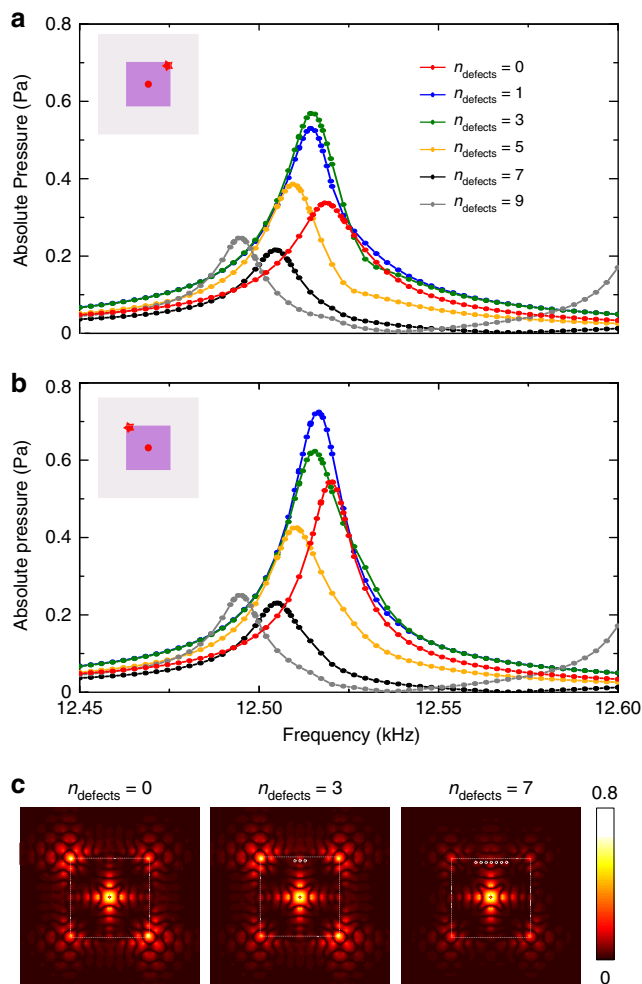


Fig. 4 Pressure spectra with growing number of interstitial defects computed at (a) the upper-right and (b) the upper-left corner of the concentric square crystal with diagonal non-Hermiticity. c Mapping the pressure distribution of the corner states in the presence of 0, 3 and 7 defects

The second non-Hermitian arrangement of the CSC is composed of parallel symmetrically gain and loss units as the magnification of Fig. 5a shows. In this scenario we obtain a mirror-like symmetry between gain and loss components that are embedded into the trivial and the non-trivial regions. The pressure spectra shown in Fig. 5b again display a perfect agreement between MST and FEM. Unlike the previously discussed corner states sustained in the diagonal non-hermiticity CSC, whose attenuating (amplifying) states confine at the diagonal (off-diagonal) corners, the parallel CSC on the contrary, binds the amplifying modes at the two right corners whereas the attenuating ones at the two left corners, as Fig. 5c shows. Furthermore, the pressure difference between the attenuating and the amplifying corner states as predicted in Fig. 5d appears to be remarkably pronounced.

From this follows that we should expect a highly selective response upon introducing defects when comparing the corner states situated at the left and right.

Indeed, the pressure spectra at the upper-right corner in Fig. 6a display a remarkable peak when compared to the opposing corner state computed in Fig. 6b. Curiously, the left corner state displays a pressure enhancement with growing interstitial defect cylinders up to $n_{\text{defects}} = 3$ above which, we witness the aforementioned

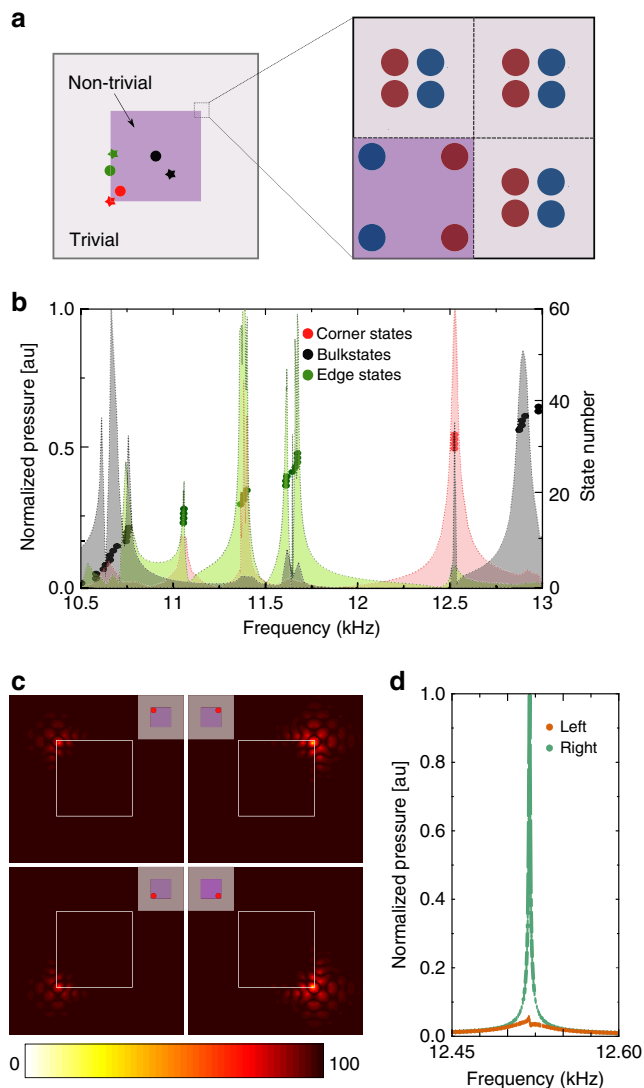


Fig. 5 Concentric square crystal (CSC) with parallel non-Hermiticity. a Magnified view of the CSC displaying the arrangement of the trivial and nontrivial regions. b Comparison between the real eigenfrequencies obtained by finite element method simulations (dots) with the normalized pressure of the excited states from the multiple scattering theory computation. c Pressure maps of all corner states. Inserts illustrate the excitation point. d Pressure difference between the amplifying and attenuating upper corner states

shift and pressure drop, however, as seen in Fig. 6c all corner states appear clearly excited in real space of the CSC.

Discussion

In conclusion, we have conducted numerical studies based on a multiple scattering theory of non-Hermitian sonic second-order topological insulators. The predicted spectral locations of the corner states in response to an acoustic point source agree very well with eigenfrequencies computations by a FEM. Our simulations further confirm the topological robustness of these corner states in the presence of interstitial cylindrical crystal defects. Interestingly, depending on the geometrical arrangement of the non-Hermitian components we are able to excite corner states of variable acoustic energy. Hence, our powerful semi-numerical predictions can reliably pave the way for the design of new acoustic devices where topological protection in combination with lossy and amplifying ingredients are in great demand.

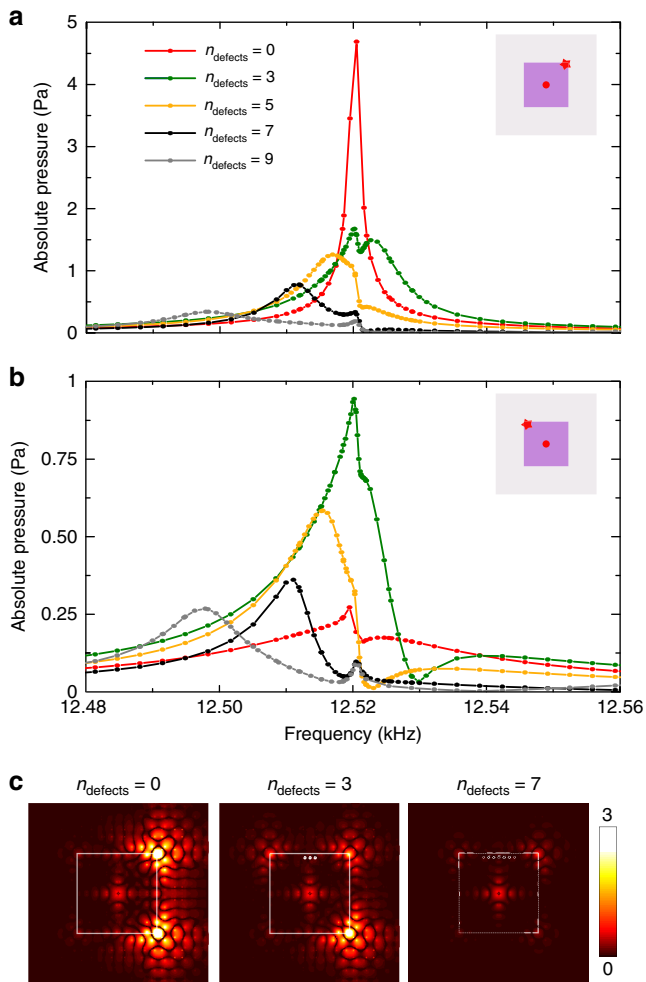


Fig. 6 Pressure spectra with growing number of interstitial defects computed at (a) the upper-left and (b) the upper-right corner of the concentric square crystal with parallel non-Hermiticity. c Mapping the pressure distribution of the corner states in the presence of 0, 3 and 7 defects

Methods

Multiple scattering theory. The semi-analytical method used to compute the pressure distribution and the resonance spectra was developed by means of the multiple scattering technique, whose formal definition has been derived in the previous result section.

Finite element method. Numerically computed eigenmodes of the SOTI were implemented using COMSOL Multiphysics, a finite-element analysis and solver software. The simulations were performed in the pressure acoustic module. The largest mesh element size was less than a tenth of the shortest incident wavelength. Plane wave radiation conditions were imposed on the exterior of the air domain to eliminate interference from the reflected waves.

Data availability

The data that support the findings of this study are available from the corresponding author on reasonable request.

Received: 16 July 2019; Accepted: 30 September 2019;

Published online: 25 October 2019

References

- Hasan, M. Z. & Kane, C. L. Colloquium: topological insulators. *Rev. Mod. Phys.* **82**, 3045 (2010).
- Qi, X.-L. & Zhang, S.-C. Topological insulators and superconductors. *Rev. Mod. Phys.* **83**, 1057 (2011).
- Bansil, A., Lin, H. & Das, T. Colloquium: topological band theory. *Rev. Mod. Phys.* **88**, 021004 (2016).
- Haldane, F. & Raghu, S. Possible realization of directional optical waveguides in photonic crystals with broken time-reversal symmetry. *Phys. Rev. Lett.* **100**, 013904 (2008).
- Wang, Z., Chong, Y., Joannopoulos, J. D. & Soljačić, M. Observation of unidirectional backscattering-immune topological electromagnetic states. *Nature* **461**, 772 (2009).
- Hafezi, M., Demler, E. A., Lukin, M. D. & Taylor, J. M. Robust optical delay lines with topological protection. *Nat. Phys.* **7**, 907 (2011).
- Poo, Y., Wu, R.-x., Lin, Z., Yang, Y. & Chan, C. Experimental realization of self-guiding unidirectional electromagnetic edge states. *Phys. Rev. Lett.* **106**, 093903 (2011).
- Yang, Z. et al. Topological acoustics. *Phys. Rev. Lett.* **114**, 114301 (2015).
- Lu, J. et al. Observation of topological valley transport of sound in sonic crystals. *Nat. Phys.* **13**, 369 (2017).
- Zhang, Z. et al. Topological creation of acoustic pseudospin multipoles in a flow-free symmetry-broken metamaterial lattice. *Phys. Rev. Lett.* **118**, 084303 (2017).
- Li, F., Huang, X., Lu, J., Ma, J. & Liu, Z. Weyl points and Fermi arcs in a chiral phononic crystal. *Nat. Phys.* **14**, 30 (2018).
- Lu, J. et al. Valley topological phases in bilayer sonic crystals. *Phys. Rev. Lett.* **120**, 116802 (2018).
- He, H. et al. Topological negative refraction of surface acoustic waves in a Weyl phononic crystal. *Nature* **560**, 61 (2018).
- Zhang, X., Xiao, M., Cheng, Y., Lu, M.-H. & Christensen, J. Topological sound. *Commun. Phys.* **1**, 97 (2018).
- Süsstrunk, R. & Huber, S. D. Observation of phononic helical edge states in a mechanical topological insulator. *Science* **349**, 47 (2015).
- Mousavi, S. H., Khanikaev, A. B. & Wang, Z. Topologically protected elastic waves in phononic metamaterials. *Nat. Commun.* **6**, 8682 (2015).
- Pal, R. K. & Ruzzene, M. Edge waves in plates with resonators: an elastic analogue of the quantum valley Hall effect. *New J. Phys.* **19**, 025001 (2017).
- Chaunsali, R., Chen, C.-W. & Yang, J. Experimental demonstration of topological waveguiding in elastic plates with local resonators. *New J. Phys.* **20**, 113036 (2018).
- Miniaci, M., Pal, R., Morvan, B. & Ruzzene, M. Experimental observation of topologically protected helical edge modes in patterned elastic plates. *Phys. Rev. X* **8**, 031074 (2018).
- Langbehn, J., Peng, Y., Trifunovic, L., von Oppen, F. & Brouwer, P. W. Reflection-symmetric second-order topological insulators and superconductors. *Phys. Rev. Lett.* **119**, 246401 (2017).
- Song, Z., Fang, Z. & Fang, C. (d-2)-dimensional edge states of rotation symmetry protected topological states. *Phys. Rev. Lett.* **119**, 246402 (2017).
- Benalcazar, W. A., Bernevig, B. A. & Hughes, T. L. Electric multipole moments, topological multipole moment pumping, and chiral hinge states in crystalline insulators. *Phys. Rev. B* **96**, 245115 (2017).
- Ezawa, M. Higher-order topological insulators and semimetals on the breathing kagome and pyrochlore lattices. *Phys. Rev. Lett.* **120**, 026801 (2018).
- Schindler, F. et al. Higher-order topological insulators. *Sci. Adv.* **4**, eaat0346 (2018).
- Imhof, S. et al. Topoelectrical-circuit realization of topological corner modes. *Nat. Phys.* **14**, 925 (2018).
- Noh, J. et al. Topological protection of photonic mid-gap defect modes. *Nat. Photonics* **12**, 408 (2018).
- Xie, B.-Y. et al. Visualization of higher-order topological insulating phases in two-dimensional dielectric photonic crystals. *Phys. Rev. Lett.* **122**, 233903 (2019).
- Chen, X.-D. et al. Direct observation of corner states in second-order topological photonic crystal slabs. *Phys. Rev. Lett.* **122**, 233902 (2019).
- Serra-Garcia, M. et al. Observation of a phononic quadrupole topological insulator. *Nature* **555**, 342 (2018).
- Xue, H., Yang, Y., Gao, F., Chong, Y. & Zhang, B. Acoustic higher-order topological insulator on a kagome lattice. *Nat. Mater.* **18**, 108 (2019).
- Ni, X., Weiner, M., Alù, A. & Khanikaev, A. B. Observation of higher-order topological acoustic states protected by generalized chiral symmetry. *Nat. Mater.* **18**, 113 (2019).
- Zhang, X. et al. Second-order topology and multidimensional topological transitions in sonic crystals. *Nat. Phys.* **15**, 582 (2019).
- Xue, H. et al. Realization of an acoustic third-order topological insulator. *Phys. Rev. Lett.* **122**, 244301 (2019).
- Weiner, M., Ni, X., Li, M., Alù, A. & Khanikaev, A. B. Demonstration of a 3rd order hierarchy of higher order topological states in a three-dimensional acoustic metamaterial. Preprint at arXiv:1903.00428 (2019).
- Zhang, X. et al. Dimensional hierarchy of higher-order topology in three-dimensional sonic crystals. Preprint at arXiv:1905.04646 (2019).

36. Fan, H., Xia, B., Tong, L., Zheng, S. & Yu, D. Elastic higher-order topological insulator with topologically protected corner states. *Phys. Rev. Lett.* **122**, 204301 (2019).
37. Zhu, X., Ramezani, H., Shi, C., Zhu, J. & Zhang, X. P t-symmetric acoustics. *Phys. Rev. X* **4**, 031042 (2014).
38. Christensen, J., Willatzen, M., Velasco, V. R. & Lu, M.-H. Parity-time synthetic phononic media. *Phys. Rev. Lett.* **116**, 207601 (2016).
39. Merkel, A., Romero-García, V., Groby, J.-P., Li, J. & Christensen, J. Unidirectional zero sonic reflection in passive PT -symmetric Willis media. *Phys. Rev. B* **98**, 201102 (2018).
40. El-Ganainy, R. et al. Non-Hermitian physics and PT symmetry. *Nat. Phys.* **14**, 11 (2018).
41. Liu, T., Zhu, X., Chen, F., Liang, S. & Zhu, J. Unidirectional wave vector manipulation in two-dimensional space with an all passive acoustic parity-time-symmetric metamaterials crystal. *Phys. Rev. Lett.* **120**, 124502 (2018).
42. Wang, M., Ye, L., Christensen, J. & Liu, Z. Valley physics in non-hermitian artificial acoustic boron nitride. *Phys. Rev. Lett.* **120**, 246601 (2018).
43. Kunst, F. K., Edvardsson, E., Budich, J. C. & Bergholtz, E. J. Biorthogonal bulk-boundary correspondence in non-Hermitian systems. *Phys. Rev. Lett.* **121**, 026808 (2018).
44. Yao, S., Song, F. & Wang, Z. Non-hermitian chern bands. *Phys. Rev. Lett.* **121**, 136802 (2018).
45. Liu, T. et al. Second-order topological phases in non-Hermitian systems. *Phys. Rev. Lett.* **122**, 076801 (2019).
46. Edvardsson, E., Kunst, F. K. & Bergholtz, E. J. Non-Hermitian extensions of higher-order topological phases and their biorthogonal bulk-boundary correspondence. *Phys. Rev. B* **99**, 081302 (2019).
47. Lee, C. H., Li, L. & Gong, J. Hybrid higher-order skin-topological modes in nonreciprocal systems. *Phys. Rev. Lett.* **123**, 016805 (2019).
48. Zhang, Z., López, M. R., Cheng, Y., Liu, X. & Christensen, J. Non-Hermitian sonic second-order topological insulator. *Phys. Rev. Lett.* **122**, 195501 (2019).
49. Martí, D. T. Towards the full control of sound with sonic crystals and acoustic metamaterials. Universidad Politécnica de Valencia. 2008
50. Liu, F., Deng, H.-Y. & Wakabayashi, K. Topological photonic crystals with zero Berry curvature. *Phys. Rev. B* **97**, 035442 (2018).
51. Fang, C., Gilbert, M. J. & Bernevig, B. A. Bulk topological invariants in noninteracting point group symmetric insulators. *Phys. Rev. B* **86**, 115112 (2012).
52. Zak, J. Berry's phase for energy bands in solids. *Phys. Rev. Lett.* **62**, 2747 (1989).
53. Xiao, M., Zhang, Z. Q. & Chan, C. T. Surface impedance and bulk band geometric phases in one-dimensional systems. *Phys. Rev. X* **4**, 021017 (2014).
54. Ota, Y. et al. Photonic crystal nanocavity based on a topological corner state. *Optica* **6**, 786 (2019).

Acknowledgements

J.C. acknowledges the support from the European Research Council (ERC) through the Starting Grant 714577 PHONOMETA and from the MINECO through a Ramón y Cajal grant (Grant No. RYC-2015-17156). D.T. acknowledges the support of MINECO through a Ramón y Cajal grant (Grant No. RYC-2016-21188) and of the Ministry of Science, Innovation and Universities through project number RTI2018-093921-A-C42.

Author contributions

J.C. conceived and led the project. M.R.-L. and D.T. developed the MST. M.R.-L. conducted all simulations based on the MST. Z.Z. conducted FEM simulations. M.R.-L. wrote the article and J.C. undertook revisions.

Competing interests

The authors declare no competing interests.

Additional information

Supplementary information is available for this paper at <https://doi.org/10.1038/s42005-019-0233-6>.

Correspondence and requests for materials should be addressed to J.C.

Reprints and permission information is available at <http://www.nature.com/reprints>

Publisher's note Springer Nature remains neutral with regard to jurisdictional claims in published maps and institutional affiliations.



Open Access This article is licensed under a Creative Commons Attribution 4.0 International License, which permits use, sharing, adaptation, distribution and reproduction in any medium or format, as long as you give appropriate credit to the original author(s) and the source, provide a link to the Creative Commons license, and indicate if changes were made. The images or other third party material in this article are included in the article's Creative Commons license, unless indicated otherwise in a credit line to the material. If material is not included in the article's Creative Commons license and your intended use is not permitted by statutory regulation or exceeds the permitted use, you will need to obtain permission directly from the copyright holder. To view a copy of this license, visit <http://creativecommons.org/licenses/by/4.0/>.

© The Author(s) 2019